

Tensor-based EDMD for the Koopman analysis of high-dimensional systems

Recent years have seen rapid advances in the data-driven analysis of dynamical systems based on Koopman operator theory – with extended dynamic mode decomposition (EDMD) being a cornerstone of the field. On the other hand, low-rank tensor product approximations – in particular the tensor train (TT) format – have become a valuable tool for the solution of large-scale problems in a number of fields. In this work, we combine EDMD and the TT format, enabling the application of EDMD to high-dimensional problems in conjunction with a large set of features. We present the construction of different TT representations of tensor-structured data arrays. Furthermore, we also derive efficient algorithms to solve the EDMD eigenvalue problem based on those representations and to project the data into a low-dimensional representation defined by the eigenvectors. We prove that there is a physical interpretation of the procedure and demonstrate its capabilities by applying the method to benchmark data sets of molecular dynamics simulation.

Keywords: Koopman operator, data-driven methods, tensor networks, tensor-train format, higher-order decomposition methods, molecular dynamics

MSC: 15A69, 37L65, 37M10, 92C40

Feliks Nüske

Center for Theoretical
Biological Physics,
Department of Chemistry,
Rice University,
Houston, TX, 77005,
United States

Patrick Gelß

Department of
Mathematics and
Computer Science,
Freie Universität Berlin,
Berlin 14195, Germany

Stefan Klus

Department of
Mathematics and
Computer Science,
Freie Universität Berlin,
Berlin 14195, Germany

Cecilia Clementi

Center for Theoretical
Biological Physics,
Department of Chemistry,
Rice University,
Houston, TX, 77005,
United States

1 Introduction

The data-driven analysis of high-dimensional dynamical systems has been a highly successful research field for several years, with applications in fluid dynamics, control theory, molecular dynamics, and many others. Most of the work along these lines has focused on the infinite-dimensional description of a system using transfer operators or Koopman operators, see [1, 2, 3, 4], which we will summarily call *evolution operators* in this paper. A host of different methods for the numerical approximation of evolution operators from simulation or measurement data have been developed, see [5] for a review and comparison. A particularly important contribution is the *extended dynamic mode decomposition* (EDMD) [6, 7], which will be the focus of this study. For reversible dynamical systems, EDMD is equivalent to the *variational approach to conformational dynamics* (VAC) [8, 9].

Much of the appeal of these techniques is due to their formulation as data-driven regression problems, which opens the door to the application of modern machine learning techniques. Examples include kernel-based formulations [10, 11] and combinations with deep learning [12]. A different avenue towards the solution of high-dimensional problems are tensor products, where functions on high-dimensional spaces are approximated in linear spaces of products of simple (often univariate) functions. The expansion coefficients of such a function form a multi-dimensional array, called a *tensor*. As the size of a tensor grows exponentially with the dimension, parametric representations (or *formats*) requiring only a manageable number of parameters need to be used. Important examples include the *canonical format* [13], the *Tucker format* [14], and the *hierarchical Tucker format* [15], with the *tensor train (TT) format* [16, 17] as an important special case of the latter. The TT format is also known under the name *matrix product states* in physics [18, 19]. The common idea behind these formats is to decompose a high-dimensional tensor into a network of lower-dimensional tensors. Several applications of tensor decompositions have shown that it is possible to tackle large-scale problems which cannot be solved using conventional numerical methods, see, e.g., [20, 21, 22, 23, 24], and especially [25] for a review of tensor product methods in quantum chemistry.

Low-rank approximations (albeit without tensors) of the matrices appearing in EDMD based on

the Nyström method were discussed in [26]. The Nyström method is conceptually related to the CUR decomposition we will employ here. Tensor-based reformulations of EDMD were proposed in [27]. Assuming the basis functions have a tensor product structure, it was shown that the matrices approximating the Perron–Frobenius or Koopman operator can directly be written in the canonical format. The resulting generalized eigenvalue problems, when converted to TT format, can be solved with the aid of power iteration methods. This, however, requires repeated rank reductions and appropriate estimates of the eigenvalues so that power iteration quickly converges. A different approach to tensor-based EDMD, based on the alternating least squares method, was suggested in [28].

Direct solution of the generalized eigenvalue problem in EDMD can be avoided using the *AMUSE* algorithm [29]. This method only requires a *singular value decomposition* (SVD) of the data matrix followed by the solution of a standard matrix eigenvalue problem. Recent work [30] has shown that such an SVD can also be computed for data matrices in TT format, operating only on the TT representation of the data. This approach was then used to compute dynamic modes of complex fluid flows as in *dynamic mode decomposition* (DMD).

In this work, we will provide an extension of the algorithm proposed in [30] to arrive at a tensor train version of AMUSE. The detailed contributions are as follows:

- First, we present two different tensor train decompositions of the data tensor corresponding to a product basis. The first one is the direct representation introduced in [24], while the second one is based on an iterative method outlined in [31], which provides a *higher-order CUR decomposition*. A detailed description of the latter method’s algorithmic realization, including several enhancements, is provided.
- Second, we derive the tensor train version of AMUSE, called *AMUSE_t*, and show that the resulting standard matrix eigenvalue problem can be set up efficiently due to orthonormality properties of the SVD.
- Third, we show that *AMUSE_t* in fact reduces the problem to performing EDMD within a subspace of the full tensor space, thus retaining a physical interpretation of the procedure. We also prove that this subspace converges in the infinite data limit.
- Finally, we demonstrate the capabilities of the proposed methods by analyzing benchmark data sets of molecular dynamics simulation, namely, deca-alanine peptide and the NTL9 protein.

The remainder of this work is structured as follows: in Section 2, we introduce the required notation and concepts, in particular Galerkin approximations of evolution operators, tensor decompositions, and higher-order tensor decompositions. The main algorithmic and theoretical contributions are presented in Section 3. Numerical results for two high-dimensional benchmark problems are then shown in Section 4, and concluding remarks and open problems follow in Section 5.

2 Fundamental concepts

In this section, we recapitulate basic concepts from dynamical systems theory and from numerical linear algebra required for the rest of the paper. First, we introduce the Galerkin approximation of evolution operators for dynamical systems in Section 2.1. This section provides the groundwork for the analysis tools developed later on. Afterwards, we change topics and discuss low-rank approximations of tensors in the tensor train format in Sections 2.2 and 2.3, while the higher CUR decomposition is presented in Section 2.4. The two strands will be connected in Section 3. Throughout the paper, vector spaces will be denoted by blackboard bold symbols (e.g., \mathbb{R}, \mathbb{V}), unless standard symbols like L^2 are used.

2.1 Galerkin projection of evolution operators

This study is concerned with the analysis of dynamical systems. Let $\mathcal{X}_t \in \mathbb{R}^d$ be a deterministic or stochastic dynamical system with unique invariant measure μ . The Koopman operator \mathcal{T}_τ on the

weighted space L_μ^2 is defined by

$$\mathcal{T}_\tau f(x) = \mathbb{E}[f(\mathcal{X}_\tau) | \mathcal{X}_0 = x]. \quad (1)$$

The operator \mathcal{T}_τ describes the time-evolution of expectation values subject to \mathcal{X}_t over a time window τ , usually called the *lag time*. If some mild assumptions are satisfied, \mathcal{T}_τ possesses a complete set of eigenfunctions φ_k such that

$$\mathcal{T}_\tau \varphi_k = \omega_k(\tau) \varphi_k = e^{-\kappa_k \tau} \varphi_k. \quad (2)$$

The eigenpairs of (2) provide a decomposition of the system into dynamical processes which decay at different rates $0 = \kappa_1 < \kappa_2 \leq \dots$, or equivalently, on different implied timescales

$$t_k := \frac{1}{\kappa_k} = -\frac{\tau}{\log(\omega_k(\tau))}, \quad k > 1, \quad (3)$$

where the second equality holds for any lag time τ . If \mathcal{X}_t is reversible with respect to μ , then \mathcal{T}_τ is self-adjoint, and its eigenvalues can also be characterized by the *Rayleigh–Ritz variational inequality*

$$\sum_{k=1}^q \langle \mathcal{T}_\tau \psi_k, \psi_k \rangle_\mu \leq \sum_{k=1}^q e^{-\kappa_k \tau}, \quad (4)$$

which holds for all sets of q mutually orthonormal functions $\{\psi_k\}_{k=1}^q$. The maximum in (4) is attained for the true eigenfunctions $\{\varphi_k\}_{k=1}^q$.

For a finite-dimensional subspace $\mathbb{V} \subset L_\mu^2$ with basis ψ_1, \dots, ψ_n , the Galerkin approximation to \mathcal{T}_τ is given by the matrix

$$K^\tau = (C^0)^+ \cdot C^\tau,$$

with $C_{ij}^\tau = \langle \psi_i, \mathcal{T}_\tau \psi_j \rangle_\mu$ and $C_{ij}^0 = \langle \psi_i, \psi_j \rangle_\mu$ [5, 7]. Approximations to the first q eigenfunctions $\varphi_1, \dots, \varphi_q$ can be found by computing the first q solutions of the eigenvalue problem

$$(C^0)^+ \cdot C^\tau \cdot v = \lambda \cdot v. \quad (5)$$

Given the eigenvectors ξ_1, \dots, ξ_q corresponding to the leading eigenvalues $\lambda_1, \dots, \lambda_q$ of (5), each vector encodes a linear combination of the basis functions. That is, for $\psi: \mathbb{R}^d \rightarrow \mathbb{R}^n$ defined by $\psi(x) = [\psi_1(x), \dots, \psi_n(x)]^\top$, the k th eigenfunction is approximated by $\tilde{\varphi}_k(x) = \xi_k^\top \psi(x)$. In the self-adjoint case, it is readily shown that the eigenvalues λ_k of (5) satisfy the *variational principle* [8].

$$\sum_{k=1}^q \lambda_k = \sum_{k=1}^q \langle \mathcal{T}_\tau \tilde{\varphi}_k, \tilde{\varphi}_k \rangle_\mu \leq \sum_{k=1}^q \omega_k(\tau) = \sum_{k=1}^q e^{-\kappa_k \tau}. \quad (6)$$

In general, the integrals required for the matrices C^0 and C^τ cannot be computed analytically, and are typically estimated from data instead. Assume we have data $x_k = \mathcal{X}_{t_k}$ sampled from the invariant measure (such as a single ergodic trajectory) and the corresponding time-lagged counterparts $y_k = \mathcal{X}_{t_k + \tau}$ with $k = 1, \dots, m$. Assembling these into data matrices $X, Y \in \mathbb{R}^{d \times m}$, where $X = [x_1, \dots, x_m]$ and $Y = [y_1, \dots, y_m]$, we define the *transformed data matrices* in $\mathbb{R}^{n \times m}$ by

$$\Psi(X) = [\psi(x_1) \quad \dots \quad \psi(x_m)] \quad \text{and} \quad \Psi(Y) = [\psi(y_1) \quad \dots \quad \psi(y_m)]. \quad (7)$$

Empirical estimates of C^0 and C^τ are then given by $\hat{C}^0 = \Psi(X) \cdot \Psi(X)^\top$ and $\hat{C}^\tau = \Psi(X) \cdot \Psi(Y)^\top$ so that we obtain the reformulated eigenvalue problem

$$(\hat{C}^0)^+ \cdot \hat{C}^\tau \cdot \xi = (\Psi(X) \cdot \Psi(X)^\top)^+ \cdot \Psi(X) \cdot \Psi(Y)^\top \cdot \xi = (\Psi(X)^\top)^+ \cdot \Psi(Y)^\top \cdot \xi = \lambda \cdot \xi, \quad (8)$$

with $\hat{C}^\tau, \hat{C}^0 \in \mathbb{R}^{n \times n}$. The data-based approximation $\hat{K}^\tau = (\hat{C}^0)^+ \cdot \hat{C}^\tau$ and the resulting eigenvalue problem (8) are known as EDMD [6, 7].

When considering a large number of basis functions, e.g., when $n \gg m$, storing the matrices C^τ and C^0 or solving the eigenvalue problem (5) may be infeasible. However, instead of computing C^τ and C^0 explicitly, we can construct a reduced matrix such that the number of rows and columns is bounded by the number of snapshots m . This is known as *AMUSE* (*algorithm for multiple unknown signals extraction*, cf. [29]), a method originally developed to solve the blind source separation problem, see Algorithm 1. A proof that the eigenvalues λ_k and corresponding eigenvectors ξ_k are indeed the solutions of the above eigenvalue problem and detailed derivations can be found in [5]. In Section 3, we will rewrite this algorithm in terms of low-rank tensor approximations.

Algorithm 1: *AMUSE for transformed data matrices.*

Input: transformed data matrices $\Psi(X)$ and $\Psi(Y)$

Output: solutions of (8) with $\hat{C}^\tau = \Psi(X) \cdot \Psi(Y)^\top$ and $\hat{C}^0 = \Psi(X) \cdot \Psi(X)^\top$

- 1: Compute a reduced SVD of $\Psi(X)$, i.e., $\Psi(X) = U \cdot \Sigma \cdot V^\top$.
 - 2: Compute $M = \Sigma^{-1} \cdot U^\top \cdot \Psi(X) \cdot \Psi(Y)^\top \cdot U \cdot \Sigma^{-1}$.
 - 3: Solve the eigenvalue problem $M \cdot w_k = \lambda_k \cdot w_k$.
 - 4: The eigenvectors are then given by $\xi_k = U \cdot \Sigma^{-1} \cdot w_k$.
-

Example 1: *To illustrate the usefulness of Galerkin projections of evolution operators, let us consider a simple low-dimensional example. We study a diffusion process*

$$d\mathcal{X}_t = -\nabla V(\mathcal{X}_t)dt + \sqrt{2\beta^{-1}}dW_t,$$

in a two-dimensional potential

$$V(x) = -2e^{-2r(x)^2} - 1.5e^{-2(r(x)-2)^2} - 1.5e^{-2(r(x)-4)^2} + e^{r(x)-6},$$

with $r(x) = r(x_1, x_2) = \sqrt{x_1^2 + x_2^2} + 0.1$, at inverse temperature $\beta = 7$. As we can see in Figure 1 (a), the potential features three circular regions where the system spends most of its time. We generate a single trajectory comprising 10000 steps using the Euler-Maruyama method, to obtain the data matrices $X, Y \in \mathbb{R}^{2 \times 10000}$, at lag time $\tau = 10$. After discretizing the domain $[-6, 6] \times [-6, 6]$ into 100×100 disjoint boxes \mathcal{B}_ℓ of equal size, we define a basis of indicator functions ψ_ℓ , $\ell = 1, \dots, 10000$, given by

$$\psi_\ell(x) = \begin{cases} 1, & \text{if } x \text{ is in box } \mathcal{B}_\ell, \\ 0, & \text{otherwise.} \end{cases}$$

The transformed data matrix $\Psi(X)$ is then of the form

$$\Psi(X) = \begin{bmatrix} \psi_1(x_1) & \cdots & \psi_1(x_m) \\ \vdots & \ddots & \vdots \\ \psi_{10000}(x_1) & \cdots & \psi_{10000}(x_m) \end{bmatrix}.$$

We apply AMUSE (Algorithm 1) to compute the eigenfunctions, and SEBA (sparse eigenbasis approximation, see [32]) in order to identify the metastable sets based on the eigenfunctions. Indeed, as shown in Figure 1 (b), the three circular regions are identified by this procedure, demonstrating how an approximation of the transfer operator can be utilized to understand the physics of the system.

2.2 Low-rank tensor representations

In what follows, we will denote tensors by bold capital letters (\mathbf{T} , \mathbf{U} , etc.), matrices by capital letters (U , V , etc.), and vectors and scalars are represented by lower case letters (x , α , etc.). The order of tensors will generally be called p , while the dimensions of the elementary vector

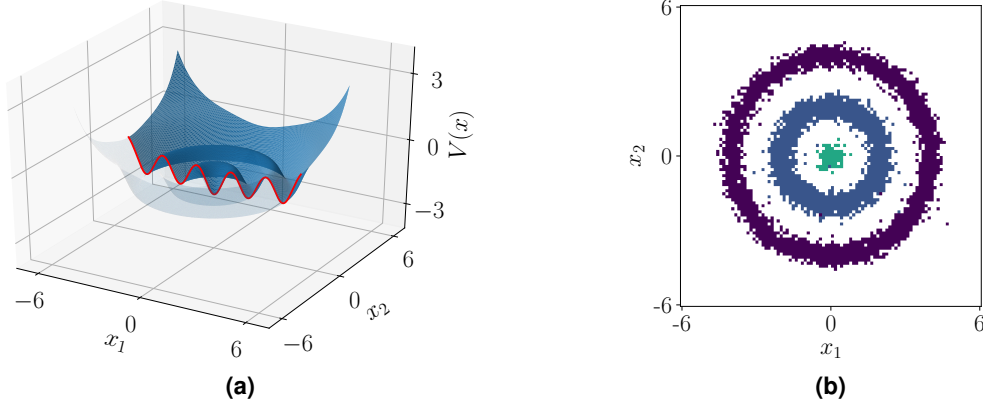


Figure 1: Example for the Galerkin projection of evolution operators: (a) Two-dimensional potential V . (b) Visualization of three metastable sets determined by AMUSE in combination with SEBA. The sets correspond to the three ring-shaped minima of the potential.

spaces (the so-called modes) are n_k , $k = 1, \dots, p$. We therefore consider tensors $\mathbf{T} \in \mathbb{R}^N$, where $N = n_1 \times \dots \times n_p$. Tensor entries are sometimes represented by multi-indices $\mathbf{i} = (i_1, \dots, i_p) \in \{1, \dots, n_1\} \times \dots \times \{1, \dots, n_p\}$, i.e., $\mathbf{T}_{\mathbf{i}} = \mathbf{T}_{i_1, \dots, i_p}$. The single-index representation of the multi-index \mathbf{i} is denoted by $\bar{\mathbf{i}} \in \{1, \dots, \prod_{k=1}^p n_k\}$. Conversely, the multi-index representation of the single-index $i \in \mathbb{N}$ is represented by \underline{i} . The tensor product is denoted by \otimes and tensor multiplication/contraction by \cdot .

We start by introducing the tensor train (TT) format, where a high-dimensional tensor is represented by the contraction of multiple low-dimensional tensors [16, 17].

Definition 1: A tensor $\mathbf{T} \in \mathbb{R}^N$ is said to be in the TT format if

$$\mathbf{T} = \sum_{l_0=1}^{r_0} \dots \sum_{l_p=1}^{r_p} \bigotimes_{k=1}^p \mathbf{T}_{l_{k-1}, :, l_k}^{(k)} = \sum_{l_0=1}^{r_0} \dots \sum_{l_p=1}^{r_p} \mathbf{T}_{l_0, :, l_1}^{(1)} \otimes \dots \otimes \mathbf{T}_{l_{p-1}, :, l_p}^{(p)}.$$

The tensors $\mathbf{T}^{(k)} \in \mathbb{R}^{r_{k-1} \times n_k \times r_k}$ of order 3 are called TT cores and the numbers r_k are called TT ranks. It holds that $r_0 = r_p = 1$ and $r_k \geq 1$ for $k = 1, \dots, p-1$.

The TT ranks r_0, \dots, r_p have a strong influence on the capability of representing a given tensor as a tensor train and determine the storage consumption of a tensor in the TT format. The storage consumption can be estimated as $O(r^2 \cdot n \cdot p)$, where r is the maximum TT rank and n the maximum mode size. Figure 2 shows the graphical representation of a tensor train, which is also called Penrose notation, see [33].

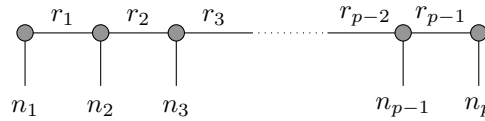


Figure 2: Graphical representation of a tensor train: A core is depicted by a circle with different arms indicating the modes of the tensor and the rank indices. The first and the last TT core are regarded as matrices due to the fact that $r_0 = r_p = 1$.

We also represent TT cores as two-dimensional arrays containing vectors as elements. For a given tensor train $\mathbf{T} \in \mathbb{R}^N$ with cores $\mathbf{T}^{(k)} \in \mathbb{R}^{r_{k-1} \times n_k \times r_k}$, a single core is written as

$$\llbracket \mathbf{T}^{(k)} \rrbracket = \begin{bmatrix} \mathbf{T}_{1, :, 1}^{(k)} & \dots & \mathbf{T}_{1, :, r_k}^{(k)} \\ \vdots & \ddots & \vdots \\ \mathbf{T}_{r_{k-1}, :, 1}^{(k)} & \dots & \mathbf{T}_{r_{k-1}, :, r_k}^{(k)} \end{bmatrix}.$$

We then use the notation $\mathbf{T} = [\mathbf{T}^{(1)}] \otimes \dots \otimes [\mathbf{T}^{(p)}]$ for representing tensor trains \mathbf{T} , cf. [22, 24, 34]. Note that this notation can be regarded as a generalization of the standard matrix multiplication. The difference is that we here compute the tensor products of the corresponding elements – which are vectors instead of scalar values – and then sum over the columns and rows, respectively.

2.3 Higher-order singular value decomposition

In theory, any tensor $\mathbf{T} \in \mathbb{R}^N$ can be converted to the TT format by reshaping and decomposing consecutive multi-dimensional arrays. For $1 \leq k \leq p-1$, the *mode- k unfolding* of the tensor \mathbf{T} is the matrix

$$\mathbf{T} \Big|_{n_1, \dots, n_k}^{n_{k+1}, \dots, n_p} \in \mathbb{R}^{(n_1 \dots n_k) \times (n_{k+1} \dots n_p)},$$

where the indices of all modes up to k are lumped into single long row indices, and all remaining indices are lumped into long column indices, i.e.,

$$\left(\mathbf{T} \Big|_{n_1, \dots, n_k}^{n_{k+1}, \dots, n_p} \right)_{\bar{\mathbf{i}}, \bar{\mathbf{j}}} = \mathbf{T}_{\mathbf{i}, \mathbf{j}} = \mathbf{T}_{i_1, \dots, i_k, i_{k+1}, \dots, i_p},$$

with $\mathbf{i} = (i_1, \dots, i_k)$ and $\mathbf{j} = (i_{k+1}, \dots, i_p)$.

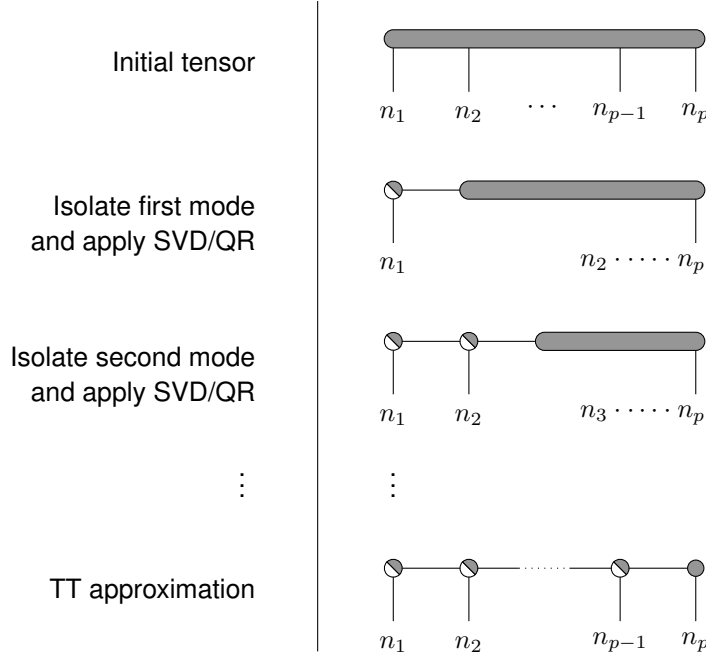


Figure 3: Conversion from full format into TT format: By reshaping and applying SVDs or QR decompositions, one mode is isolated in every step.

The idea now is to successively apply common matrix factorizations, e.g., singular value decompositions, to different unfoldings of the tensor. It was shown in [16, 17] that the procedure visualized in Figure 3 yields an exact TT representation, i.e., the contraction of the TT cores would result in the initial tensor (neglecting numerical errors). In each step, we decompose the residual tensor $\mathbf{T}_k \in \mathbb{R}^{r_{k-1} \times n_k \times \dots \times n_p}$, where r_{k-1} is the corresponding TT rank. That is, we compute an SVD (or QR decomposition) of the unfolding

$$T_k = \mathbf{T}_k \Big|_{r_{k-1}, n_k}^{n_{k+1}, \dots, n_p}, \quad (9)$$

for $k = 1, \dots, p-1$. Using reduced SVDs for the decomposition, i.e., $T_k = U_k \cdot \Sigma_k \cdot V_k^\top$ with $\Sigma_k \in \mathbb{R}^{r_k \times r_k}$, the matrix U_k reshaped as a tensor of size $\mathbb{R}^{r_{k-1} \times n_k \times r_k}$ constitutes the k th core

$\mathbf{T}^{(k)}$, with r_k being the TT rank. The resulting core is then *left-orthonormal*, i.e.,

$$\left(\mathbf{T}^{(k)} \begin{array}{c} r_k \\ r_{k-1}, n_k \end{array} \right)^\top \cdot \left(\mathbf{T}^{(k)} \begin{array}{c} r_k \\ r_{k-1}, n_k \end{array} \right) = U_k^\top \cdot U_k = \text{Id} \in \mathbb{R}^{r_k \times r_k},$$

where Id denotes the identity matrix. Orthonormality of TT cores is depicted by half-filled circles, cf. Figure 3. The non-orthonormal part $\Sigma_k \cdot V_k^\top$ defines the next residual tensor.

It was also shown that, if the SVDs are truncated in each step using a relative error tolerance ε , then the relative error (in the Frobenius norm) of the TT decomposition is bounded by $\sqrt{p-1} \varepsilon$. This algorithm is generally referred to as *higher-order singular value decomposition* (HOSVD). As we have shown in [30], sequential SVDs can also be used to compute pseudoinverses of tensor unfoldings directly in the TT format. The specific application of this method will be explained in more detail in Section 3.

2.4 Higher-order CUR decomposition

In case the initial tensor for the HOSVD method described in Section 2.3 cannot be stored entirely, an alternative isolation technique for the modes has to be used, since all SVDs require the whole residual tensor as input. If we assume that we have an explicit expression for each element of the initial tensor, SVDs can be replaced by so-called *CUR decompositions*, see [35, 36], within the HOSVD algorithm.

For a matrix $M \in \mathbb{R}^{m \times n}$, a CUR decomposition consists of index sets I, J , as well as submatrices $C = M_{:,J}$, $U = M_{I,J}$, and $R = M_{I,:}$, such that $M \approx C \cdot U^{-1} \cdot R$, see Figure 4.

$$\left[\begin{array}{cccc} \cdot & \cdot & \cdot & \cdot \\ \cdot & \cdot & \cdot & \cdot \\ \cdot & \cdot & \cdot & \cdot \\ \cdot & \cdot & \cdot & \cdot \end{array} \right] \approx \left[\begin{array}{c} | \\ | \\ | \\ | \end{array} \right] \cdot \left[\begin{array}{ccc} \times & \times & \times \\ \times & \times & \times \\ \times & \times & \times \end{array} \right]^{-1} \cdot \left[\begin{array}{cccc} \text{---} & \text{---} & \text{---} & \text{---} \\ \text{---} & \text{---} & \text{---} & \text{---} \\ \text{---} & \text{---} & \text{---} & \text{---} \end{array} \right]$$

Figure 4: *CUR decomposition: The matrix on the left-hand side is approximated by the matrix product $C \cdot U^{-1} \cdot R$, where C (blue lines) is a column subset, R (green lines) is a row subset, and U (red crosses) is the intersection matrix.*

As described in [31], the CUR decomposition can be generalized to a tensor by replacing the SVDs in the HOSVD algorithm by CUR decompositions. Given suitable row and column sets $\mathbf{I}_k, \mathbf{J}_k$ of sizes r_k , the unfolded residual tensor T_k in (9) is decomposed by the CUR $T_k = C_k \cdot U_k^{-1} \cdot R_k$ instead of an SVD. The k th core is then defined as a reshape of $C_k \cdot U_k^{-1}$, while R_k turns into the next residual tensor.

In the matrix case, there are different methods to find optimal sets of rows and columns, cf. [37]. To prepare for the tensor case, we only need to consider the following subproblem for a matrix $M \in \mathbb{R}^{m \times n}$: given a set of column indices $J = \{j_1, \dots, j_r\}$ with $r \leq \min(m, n)$ (and $M_{:,J}$ having full column rank), we wish to find an optimal subset of row indices $I = \{i_1, \dots, i_r\}$. Based on the *maximum-volume principle* introduced in [38], this problem can be solved by applying Algorithm 2 to $M_{:,J}$, so that the infinity norm of $M - M_{:,J} \cdot M_{I,J}^{-1} \cdot M_{I,:}$ is minimized over I , see [38, 39]. In other words, $M_{I,J}$ is a *dominant submatrix* of $M_{:,J}$.

In order to find the first set of linearly independent rows in Line 2 of Algorithm 2, one could, for instance, apply a QR decomposition with column pivoting to M^\top . In Section 3.2, we will iteratively use Algorithm 2 to compute CUR decompositions of submatrices of tensors that are given entry-wise.

3 Tensor-based EDMD

Let us now combine the techniques for the data-driven approximation of evolution operators, see Section 2.1, and for the low-rank approximation of multi-dimensional arrays, see Sections 2.2

Algorithm 2: *Maximum-volume principle.*

Input: matrix $M \in \mathbb{R}^{m \times n}$ with $m \geq n$, maximum number of iterations $N \geq 1$, tolerance $\varepsilon > 0$
Output: row set $I = \{i_1, \dots, i_r\}$ with $r \leq n$ s.t. $M_{I,:}$ is a (quasi-)dominant submatrix

- 1: Set $k = 1$ and $\delta > 1 + \varepsilon$.
 - 2: Find linearly independent rows $I = \{i_1, \dots, i_r\}$ of M (with r being as large as possible).
 - 3: **if** $r < n$ **then** keep the first r columns of M and disregard the rest.
 - 4: **while** $\delta > 1 + \varepsilon$ and $k \leq N$ **do**
 - 5: Set $U = M_{I,:}$ and compute $\widehat{M} = M \cdot U^{-1}$.
 - 6: Set $(p, q) = \arg \max_{i,j} |\widehat{M}_{i,j}|$ and replace i_q by p in I .
 - 7: Set $\delta = |\widehat{M}_{p,q}|$ and increase k by 1.
-

to 2.4. We consider data matrices $X, Y \in \mathbb{R}^{d \times m}$ originating from a stochastic process \mathcal{X}_t , and a set of basis functions ψ_1, \dots, ψ_p with $\psi_k: \mathbb{R}^d \rightarrow \mathbb{R}^{n_k}$ where $n_k \in \mathbb{N}$ for $k = 1, \dots, p$. Let $\mathbb{V}^k = \text{span}\{\psi_{k,1}, \dots, \psi_{k,n_k}\}$ denote the n_k -dimensional subspaces spanned by the elementary basis functions $\psi_{k,1}, \dots, \psi_{k,n_k}$. We consider the Galerkin projection (5) on the tensor product $\mathbb{V} := \mathbb{V}^1 \otimes \dots \otimes \mathbb{V}^p \subset L_\mu^2$, which is a subspace of dimension $n_1 \cdot \dots \cdot n_p$. We then reformulate the eigenvalue problem (5) using tensors $\mathbf{C}^\tau, \mathbf{C}^0 \in \mathbb{R}^{N \times N}$ with $N = n_1 \times \dots \times n_p$. That is, the Galerkin matrices C^τ and C^0 are replaced by tensor-structured linear operators given by

$$\mathbf{C}_{ij}^\tau = \langle \Psi_i, \mathcal{T}_\tau \Psi_j \rangle_\mu \quad \text{and} \quad \mathbf{C}_{ij}^0 = \langle \Psi_i, \Psi_j \rangle_\mu,$$

where $\Psi_i = \prod_{k=1}^p \psi_{k,i_k}$ for each multi-index $\mathbf{i} = (i_1, \dots, i_p)$. This results in the tensorized eigenvalue problem

$$(\mathbf{C}^0)^\dagger \cdot \mathbf{C}^\tau \cdot \mathbf{V} = \lambda \cdot \mathbf{V}, \quad (10)$$

where \mathbf{V} is a tensor in \mathbb{R}^N .

In what follows, we will denote the tensor-based counterparts of the transformed data matrices given in (7) by $\Psi(X)$ and $\Psi(Y)$, respectively. These *transformed data tensors* can then be used to obtain empirical estimates of \mathbf{C}^τ and \mathbf{C}^0 , i.e., $\widehat{\mathbf{C}}^\tau = \Psi(X) \cdot \Psi(Y)^\top$ and $\widehat{\mathbf{C}}^0 = \Psi(X) \cdot \Psi(X)^\top$, and to construct the reformulated eigenvalue problem as described in (8).

The combination of tensor-based basis decompositions (Section 3.1) – either using HOSVD (Section 2.3) or HOCUR (Sections 2.4 and 3.2) – with tensor-based AMUSE (Sections 3.3 and 3.4) is summarized under the term *tensor-based EDMD* (tEDMD).

3.1 Basis decompositions

As we have shown in [24], the tensor train format can be used to represent transformed data tensors. As above, let $x \in \mathbb{R}^d$ be a vector and $\psi_k: \mathbb{R}^d \rightarrow \mathbb{R}^{n_k}$, $k = 1, \dots, p$, basis functions. We consider the rank-one tensors

$$\Psi(x) = \psi_1(x) \otimes \dots \otimes \psi_p(x) = \begin{bmatrix} \psi_{1,1}(x) \\ \vdots \\ \psi_{1,n_1}(x) \end{bmatrix} \otimes \dots \otimes \begin{bmatrix} \psi_{p,1}(x) \\ \vdots \\ \psi_{p,n_p}(x) \end{bmatrix} \in \mathbb{R}^{n_1 \times n_2 \times \dots \times n_p}. \quad (11)$$

For m different vectors stored in a data matrix $X = [x_1, \dots, x_m] \in \mathbb{R}^{d \times m}$, we now construct transformed data tensors $\Psi(X) \in \mathbb{R}^{n_1 \times \dots \times n_p \times m}$ with $\Psi(X)_{:, \dots, :, k} = \Psi(x_k)$. This is achieved by adding the rank-one decompositions given in (11) for all vectors x_1, \dots, x_m and taking the tensor

product with an additional unit vector. The result is the following TT decomposition:

$$\begin{aligned}
\Psi(X) &= \sum_{k=1}^m \Psi(x_k) \otimes e_k \\
&= \sum_{k=1}^m \psi_1(x_k) \otimes \cdots \otimes \psi_p(x_k) \otimes e_k \\
&= \begin{bmatrix} \psi_1(x_1) & \cdots & \psi_1(x_m) \end{bmatrix} \otimes \begin{bmatrix} \psi_2(x_1) & & 0 \\ & \ddots & \\ 0 & & \psi_2(x_m) \end{bmatrix} \otimes \cdots \\
&\quad \cdots \otimes \begin{bmatrix} \psi_p(x_1) & & 0 \\ & \ddots & \\ 0 & & \psi_p(x_m) \end{bmatrix} \otimes \begin{bmatrix} e_1 \\ \vdots \\ e_m \end{bmatrix} \\
&=: \begin{bmatrix} \Psi^{(1)}(X) \end{bmatrix} \otimes \begin{bmatrix} \Psi^{(2)}(X) \end{bmatrix} \otimes \cdots \otimes \begin{bmatrix} \Psi^{(p)}(X) \end{bmatrix} \otimes \begin{bmatrix} \Psi^{(p+1)}(X) \end{bmatrix},
\end{aligned} \tag{12}$$

where e_k , $k = 1, \dots, m$, denote the unit vectors of the standard basis in the m -dimensional Euclidean space. Let us note that the so-called *coordinate-major* and *function-major* basis decompositions, introduced in [24], are special cases of the more general decomposition given in (11) and (12).

The matrix-based counterpart of $\Psi(X)$, see (7), would be given by the mode- p unfolding

$$\Psi(X) = \Psi(X) \Big|_{n_1, \dots, n_p}^m, \tag{13}$$

that is, modes n_1, \dots, n_p represent row indices of the unfolding, and mode m is the column index. To account for this, we slightly change the graphical representation for transformed data tensors and transpose the last TT core, as shown in Figure 5 (a).

Example 2: Let us again consider our guiding example from Section 2.1. For the construction of the transformed data matrices we chose indicator functions on two-dimensional boxes in the domain $[-6, 6] \times [-6, 6]$. These basis functions can be expressed as products of one-dimensional basis functions. Since the domain is discretized into disjoint boxes of equal size, each box \mathcal{B}_ℓ , $\ell = 1, \dots, 10000$, is given by

$$\mathcal{B}_\ell = \{x = (x_1, x_2) \in \mathbb{R}^2 : x_1 \in I_{\ell_1} \wedge x_2 \in I_{\ell_2}\}$$

with $\ell = (\ell_1, \ell_2)$, $1 \leq \ell_1, \ell_2 \leq 100$, and corresponding intervals $I_{\ell_1}, I_{\ell_2} \subset [-6, 6]$. Thus, we can write ψ_ℓ as the product of two one-dimensional indicator functions, i.e.,

$$\psi_\ell(x) = \mathbb{1}_{I_{\ell_1}}(x_1) \cdot \mathbb{1}_{I_{\ell_2}}(x_2).$$

It follows that the corresponding transformed data tensor $\Psi(X)$ can be expressed as

$$\Psi(X) = \sum_{k=1}^m \begin{bmatrix} \mathbb{1}_{I_1}(x_{k,1}) \\ \vdots \\ \mathbb{1}_{I_{100}}(x_{k,1}) \end{bmatrix} \otimes \begin{bmatrix} \mathbb{1}_{I_1}(x_{k,2}) \\ \vdots \\ \mathbb{1}_{I_{100}}(x_{k,2}) \end{bmatrix} \otimes e_k$$

for any snapshot matrix $X = [x_1, \dots, x_m]$.

3.2 HOCUR for transformed data tensors

Next, we present an alternative construction of a TT representation for a transformed data tensor $\Psi(X)$ based on the HOCUR decomposition discussed in Section 2.4. The motivation is that the construction of $\Psi(X)$ as described in Section 3.1 may still be infeasible in practice due to a large number of basis functions or snapshots. We will see in the next section that, in order to

apply EDMD to a tensor-structured basis set, we need to apply orthonormalization techniques to the TT representation (12). Even if the cores of the initial construction (12) can be stored in a sparse format, orthonormalization is likely to produce dense TT cores. Thus, unless the TT ranks significantly decrease during the orthonormalization procedure, the resulting tensor train may easily become too complex for efficient computations.

Algorithm 3 is a combination of different techniques from [31, 38, 39], specifically adapted to transformed data tensors as described in Section 3.1. As suggested in [31], Algorithm 3 successively updates the rows sets of the unfolded residual tensors during a forward loop, while all column sets are fixed. Then, column sets are updated during a backward loop, with all row sets fixed, and the entire procedure is repeated until convergence. The key insight, used in lines 5 – 9 and 13 – 14, is that each update only operates on a small subtensor which is easily evaluated. Assume we are given a row set $\mathbf{I} = \mathbf{I}_q = \{\mathbf{i}_1, \dots, \mathbf{i}_{r_q}\}$ of multi-indices comprising modes n_1, \dots, n_q , and a column set $\mathbf{J} = \mathbf{J}_{q+2} = \{\mathbf{j}_1, \dots, \mathbf{j}_s\}$ of multi-indices comprising modes n_{q+2}, \dots, n_p, m :

$$\begin{aligned} \mathbf{i}_1, \dots, \mathbf{i}_{r_q} &\in \{1, \dots, n_1\} \times \dots \times \{1, \dots, n_q\}, \\ \mathbf{j}_1, \dots, \mathbf{j}_s &\in \{1, \dots, n_{q+2}\} \times \dots \times \{1, \dots, n_p\} \times \{1, \dots, m\}. \end{aligned}$$

Then, a new extended row set comprising the first $q+1$ modes

$$\mathbf{i}_1, \dots, \mathbf{i}_{r_{q+1}} \in \{1, \dots, n_1\} \times \dots \times \{1, \dots, n_{q+1}\},$$

can be obtained by applying Algorithm 2 to the submatrix $\Psi(X)_{|\mathbf{I}, \mathbf{J}} \in \mathbb{R}^{r_q \cdot n_{q+1} \times s}$, given by

$$\Psi(X)_{|\mathbf{I}, \mathbf{J}} = \begin{bmatrix} \Psi(X)_{\mathbf{i}_1, :; \mathbf{j}_1} & \dots & \Psi(X)_{\mathbf{i}_1, :; \mathbf{j}_s} \\ \vdots & \ddots & \vdots \\ \Psi(X)_{\mathbf{i}_{r_q}, :; \mathbf{j}_1} & \dots & \Psi(X)_{\mathbf{i}_{r_q}, :; \mathbf{j}_s} \end{bmatrix}. \quad (14)$$

This matrix is easily set up using basis function evaluations. More precisely, given multi-indices $\mathbf{i} = (i_1, \dots, i_q) \in \mathbf{I}$ and $\mathbf{j} = (i_{q+2}, \dots, i_p, k) \in \mathbf{J}$, entries $\Psi(X)_{\mathbf{i}, :; \mathbf{j}}$ of $\Psi(X)_{|\mathbf{I}, \mathbf{J}}$ are given by

$$\begin{aligned} \Psi(X)_{\mathbf{i}, :; \mathbf{j}} &= \Psi(X)_{i_1, \dots, i_q, :; i_{q+2}, \dots, i_p, k} \\ &= \underbrace{\psi_{1, i_1}(x_k) \cdot \dots \cdot \psi_{q, i_q}(x_k)}_{\in \mathbb{R}} \cdot \underbrace{\psi_{q+1}(x_k)}_{\in \mathbb{R}^{n_{q+1}}} \cdot \underbrace{\psi_{q+2, i_{q+2}}(x_k) \cdot \dots \cdot \psi_{p, i_p}(x_k)}_{\in \mathbb{R}}. \end{aligned}$$

Note that the last entry of the column index \mathbf{j} determines the snapshot x_k where the product is evaluated.

Let us elaborate on a few more details of Algorithm 3. First, note that multi-index sets for the construction of the submatrices $\Psi(X)_{|\mathbf{I}, \mathbf{J}}$ are nested sets by construction. In Line 10, after each application of Algorithm 2, the resulting single-index set $I = \{i_1, \dots, i_{r_{q+1}}\}$ needs to be converted into a multi-index row set for modes n_1, \dots, n_{q+1} . Given a multi-index row set $\mathbf{I}_q = \{\mathbf{i}_1, \dots, \mathbf{i}_{r_q}\}$ as above, each row of $\Psi(X)_{|\mathbf{I}_q, \mathbf{J}_{q+2}}$ can naturally be associated with a multi-index $(k_1, k_2) \in \{1, \dots, r_q\} \times \{1, \dots, n_{q+1}\}$. Hence, we map each single-index $i_k \in I$ to a multi-index $\underline{i}_k = (\underline{i}_{k,1}, \underline{i}_{k,2})$ in $\{1, \dots, r_q\} \times \{1, \dots, n_{q+1}\}$, and then define the extended multi-index row set

$$\mathbf{I}_{q+1} = \{(\underline{i}_{\underline{i}_{1,1}}, \underline{i}_{1,2}), \dots, (\underline{i}_{\underline{i}_{r_{q+1},1}}, \underline{i}_{r_{q+1},2})\}. \quad (15)$$

Column sets are updated analogously in Line 15 of Algorithm 3.

Second, the algorithm requires initial column sets which are generated in Line 2. While it was suggested in [31] to pick these columns at random, we build them up recursively to ensure the column sets are also nested. Starting from $\mathbf{J}_{p+2} = \{\emptyset\}$, column set \mathbf{J}_q is obtained by simply selecting the first $\min(\alpha \cdot r_q, n_{q+1} \cdot r_{q+1})$ indices out of the index set $\{1, \dots, n_{q+1} \cdot r_{q+1}\}$, and then joining them with multi-index column set \mathbf{J}_{q+1} as described above in (15). In practice, we found it helpful to select a rather large number of columns at this point, as these initial columns would often be highly redundant. The parameter α can be tuned to ensure enough columns are selected during the initialization stage.

Third, similar to Algorithm 2, we need to find index sets of linearly independent columns of the matrices $\Psi(X)_{|\mathbf{I}, \mathbf{J}}$ during the first iteration, see Line 7. This can again be done by applying QR

Algorithm 3: Higher-order CUR decomposition.

Input:	data matrix $X = [x_1, \dots, x_m] \in \mathbb{R}^{d \times m}$, basis functions ψ_{i,j_i} , $i = 1, \dots, p$, $j_i = 1, \dots, n_i$, maximum ranks r_1, \dots, r_p with $r_q \leq n_{q+1} \cdot r_{q+1}$, number of iterations N , multiplier $\alpha > 1$
Output:	TT approximation of the transformed data tensor $\Psi(X)$

- 1: Set $n_{p+1} = m$, $r_0 = r_{p+1} = 1$, and $\mathbf{I}_0 = \{\emptyset\}$.
- 2: Define initial multi-index column sets $\mathbf{J}_2, \dots, \mathbf{J}_{p+2}$.
- 3: **for** $k = 1, \dots, N$ **do**
- 4: **for** $l = 1, \dots, p$ **do** (First half sweep)
- 5: Extract submatrix $M = \Psi(X)_{|\mathbf{I}_{l-1}, \mathbf{J}_{l+1}|}$, see (14).
- 6: **if** $k = 1$ **then**
- 7: Find set of linearly independent columns J of M with $|J| \leq r_l$.
- 8: Set M to $M_{:,J}$ and r_l to $|J|$.
- 9: Apply Algorithm 2 to M to extract row set I .
- 10: Compute multi-index row set \mathbf{I}_l from \mathbf{I}_{l-1} and I , see (15).
- 11: Define core $\Psi(X)^{(l)}$ as $M \cdot M_{I,:}^{-1}$ reshaped as $\mathbb{R}^{r_{l-1} \times n_l \times r_l}$.
- 12: **for** $l = p+1, \dots, 2$ **do** (Second half sweep)
- 13: Extract submatrix $M = \Psi(X)_{|\mathbf{I}_{l-1}, \mathbf{J}_{l+1}|}$ and reshape as $\mathbb{R}^{r_{l-1} \times n_l \times r_l}$.
- 14: Apply Algorithm 2 to M^\top to extract column set J and set $r_{l-1} = |J|$.
- 15: Compute multi-index column set \mathbf{J}_l from J and \mathbf{J}_{l+1} .
- 16: Define core $\Psi(X)^{(l)}$ as $M_{:,J}^{-1} \cdot M$ reshaped as $\mathbb{R}^{r_{l-1} \times n_l \times r_l}$.
- 17: Define first core $\Psi(X)^{(1)}$ as $\Psi(X)_{|\mathbf{I}_0, \mathbf{J}_2|}$ reshaped as $\mathbb{R}^{1 \times n_1 \times r_1}$.

decompositions with column pivoting. And finally, the cores of the TT approximation of $\Psi(X)$ are updated in Lines 11 and 16, by multiplication of parts of the determined CUR decomposition. In the notation used in Section 2.4, the updated cores are given by tensor foldings of $C \cdot U^{-1}$ and $U^{-1} \cdot R$, respectively.

Example 3: After showing how to decompose the basis functions of our guiding example in Example 2, we can now apply HOSVD/HOCUR to the simulation data. By applying the HOSVD method with different thresholds to the tensor train defined by (12), we are able to construct TT approximations of $\Psi(X)$. The TT ranks of the decompositions as well as the approximation errors depend on the relative truncation threshold ε for the SVDs. In Table 1, we show the ranks and the relative Frobenius norm approximation error

$$\frac{\left\| \Psi(X) - \Psi_\varepsilon(X) \right\|_{10000, 100, 100}_F}{\left\| \Psi(X) \right\|_F}$$

between $\Psi(X)$ and its TT approximation $\Psi_\varepsilon(X) \in \mathbb{R}^{100 \times 100 \times 10000}$ for a given tolerance ε . Comparing the approximation errors for $\varepsilon = 0$ and $\varepsilon = 1e-12$, we see that the transformed data matrix can be almost exactly represented in the TT format with ranks $[1, 76, 2389, 1]$. Here, the second last rank is simply equal to the number of boxes which were visited by the trajectory stored in the data matrix X . Due to the binary structure of the transformed data matrix, the TT ranks do not change when using thresholds between $1e-12$ and $1e-2$. However, using a threshold of $1e-1$ then results in only slightly lower TT ranks but, at the same time, in a significant decline of approximation quality. A similar trend can be observed when applying the HOCUR decomposition to $\Psi(X)$, at maximal ranks on the same order as the number of visited boxes (see lower panel of Table 1).

Note that this is only an illustrative toy example, we merely aim to show here that HOSVD and HOCUR are in principle able to provide TT decompositions of transformed data matrices. The selected basis set is not comprised of smooth functions and thus is not amenable to low-rank approximations. We will employ basis sets with better regularity properties in the applications presented in Section 4.

Table 1: *TT approximation of transformed data tensors using HOSVD and HOCUR: For different thresholds (HOSVD) and maximum ranks (HOCUR), the resulting ranks of the TT representation and the corresponding approximation errors are shown.*

Method	Threshold/maximum rank	TT ranks	Approximation error
HOSVD	0	[1, 100, 10000, 1]	4.32e−15
	1e−12	[1, 76, 2389, 1]	3.55e−15
	1e−01	[1, 74, 2387, 1]	1.41e−02
HOCUR	2400	[1, 75, 2388, 1]	1.00e−02
	2375	[1, 75, 2375, 1]	3.74e−02
	2350	[1, 75, 2350, 1]	6.32e−02

3.3 Global SVD and pseudoinverse

Solving the eigenvalue problem (10) by the AMUSE Algorithm 1 requires an SVD of the transformed data tensor $\Psi(X)$, or of its mode- p unfolding (13). In [30], we proposed a method to directly compute the singular value decomposition of a tensor train without leaving the TT format. Applied to transformed data tensors as described in Section 3.1, the method provides a tensor train in form of a segment $\mathbf{U} \in \mathbb{R}^{n_1 \times \dots \times n_p \times r}$, a diagonal coupling matrix $\Sigma \in \mathbb{R}^{r \times r}$, and an orthonormal $V \in \mathbb{R}^{m \times r}$ representing the last core. The dimension r is the TT rank between the two last cores. Just like a standard SVD of a matrix, \mathbf{U} , Σ , and V then satisfy the following properties:

- i) $\Psi(X) = \mathbf{U} \cdot \Sigma \cdot V^\top$,
- ii) $\mathbf{U}^\top \cdot \mathbf{U} = V^\top \cdot V = \text{Id} \in \mathbb{R}^{r \times r}$,
- iii) $\Sigma \in \mathbb{R}^{r \times r}$ is a diagonal matrix.

The method proceeds as follows: first, we right-orthonormalize the last TT core $\Psi^{(p+1)}(X)$ using a (truncated) SVD and shift the non-orthonormal parts to the preceding core. Then, similarly to the HOSVD algorithm, we left-orthonormalize the TT cores $\Psi^{(1)}(X), \dots, \Psi^{(p-1)}(X)$, cf. Figure 3, again using truncated SVDs if required. Afterwards, we decompose the TT core $\Psi^{(p)}(X)$, but this time retain the diagonal matrix containing the singular values and only shift the right-orthonormal matrix to the last core $\Psi^{(p+1)}(X)$. This provides the components of the global SVD as shown in Figure 5 (a). We remark that the global SVD procedure also allows to calculate the pseudoinverse of a tensor train, see Figure 5 (b) and [30].

3.4 AMUSEt

Let us now come to the main method of this paper. In order to solve the eigenvalue problem (10) with empirical estimates

$$\hat{\mathbf{C}}^\tau = \Psi(X) \cdot \Psi(Y)^\top \quad \text{and} \quad \hat{\mathbf{C}}^0 = \Psi(X) \cdot \Psi(X)^\top,$$

where $\Psi(X)$ and $\Psi(Y)$ are given in TT format, we apply the tensor-based counterpart of the AMUSE algorithm [29] discussed in Section 2.1. Instead of solving the eigenvalue problem in the TT format, cf. [22, 40], we construct a reduced eigenvalue problem with the same spectrum as (10). The resulting tensor-based method will be called *AMUSEt* (*AMUSE on tensors*).

The basic idea is to first apply the global SVD to $\Psi(X)$, and then to compute the reduced matrix M as in Line 2 of Algorithm 1, which leads to the contraction of a tensor network similar to the DMD case described in [30]. However, the complexity of AMUSEt can be reduced further in many cases. Oftentimes, we consider snapshot matrices $X, Y \in \mathbb{R}^{d \times m}$, which are extracted from a trajectory data matrix $Z \in \mathbb{R}^{d \times \tilde{m}}$, $\tilde{m} > m$ and share a large number of common snapshot vectors. Instead of constructing the transformed data tensors separately, we can construct the TT decomposition of $\Psi(Z)$ and then simply restrict the last TT core to the respective time steps

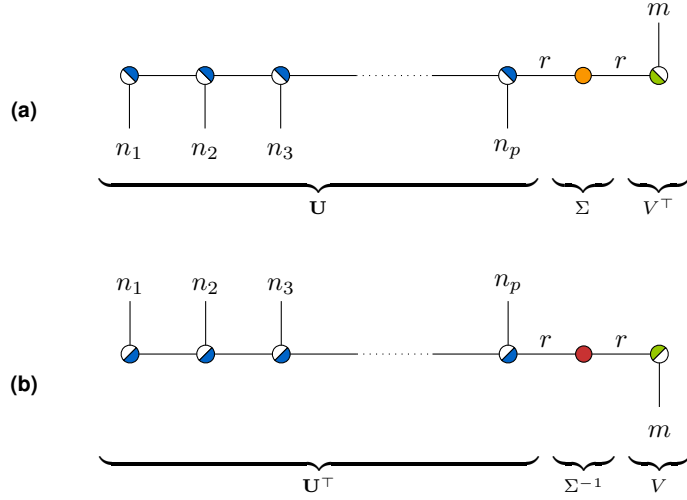


Figure 5: Global SVD and pseudoinverse in TT format: (a) Global SVD of a transformed data tensor $\Psi(X)$ with components \mathbf{U} (half-filled circles in blue), Σ (orange circle), and \mathbf{V} (half-filled circle in green). The first p modes depict the row indices while the last mode depicts the column index. (b) Pseudoinverse of $\Psi(X)$, where the cores of \mathbf{U} and \mathbf{V} are transposed and Σ is replaced by its inverse (red circle).

in order to obtain the representations for $\Psi(X)$ and $\Psi(Y)$. That is, given the data matrix Z , and index sets I_X, I_Y such that $X = Z_{:,I_X}$ and $Y = Z_{:,I_Y}$, we construct

$$\Psi(Z) = \llbracket \Psi^{(1)}(Z) \rrbracket \otimes \llbracket \Psi^{(2)}(Z) \rrbracket \otimes \dots \otimes \llbracket \Psi^{(p)}(Z) \rrbracket \otimes \llbracket \Psi^{(p+1)}(Z) \rrbracket$$

either by the direct approach, see Section 3.1, or by applying Algorithm 3. Then, the tensor trains $\Psi(X)$ and $\Psi(Y)$ are given by

$$\Psi(X) = \llbracket \Psi^{(1)}(Z) \rrbracket \otimes \llbracket \Psi^{(2)}(Z) \rrbracket \otimes \dots \otimes \llbracket \Psi^{(p)}(Z) \rrbracket \otimes \left[\left(\Psi^{(p+1)}(Z) \right)_{:,I_X,1} \right]$$

and

$$\Psi(Y) = \llbracket \Psi^{(1)}(Z) \rrbracket \otimes \llbracket \Psi^{(2)}(Z) \rrbracket \otimes \dots \otimes \llbracket \Psi^{(p)}(Z) \rrbracket \otimes \left[\left(\Psi^{(p+1)}(Z) \right)_{:,I_Y,1} \right].$$

Hence, we first left-orthonormalize the tensor train $\Psi(Z)$ and then extract $\Psi(X)$ as well as $\Psi(Y)$ by restricting the last core to the corresponding indices. Additionally, we construct a global SVD of $\Psi(X)$ in the form of $\mathbf{U} \cdot U_X \cdot \Sigma_X \cdot V_X^\top$. That is, we compute an SVD of the last core of $\Psi(X)$. The result is then a tensor network similar to the one shown in Figure 5 (a). The respective transformations of the considered tensor trains are visualized in Figure 6.

The reduced matrix is given by

$$M = \Sigma^{-1} \cdot U_X^\top \cdot \mathbf{U}^\top \cdot \Psi(X) \cdot \Psi(Y)^\top \cdot \mathbf{U} \cdot U_X \cdot \Sigma^{-1}. \quad (16)$$

Figure 7 shows the corresponding tensor network. By construction, $\Psi(X)$ and $\Psi(Y)$ share the same segment \mathbf{U} . Since the cores of \mathbf{U} (as well as U_X) are left-orthonormal, most of the contractions cancel out, and only four matrices remain, namely V_X^\top , M_Y , U_X , and Σ^{-1} . Thus, the reduced matrix M is simply constructed by the multiplication of these matrices.

Furthermore, we are typically not interested in the full eigentensors but rather in the projections of the data onto approximate eigenfunctions of the Koopman operator (1). Given the q leading eigenvectors of the reduced matrix M in form of a matrix $W = [w_1, \dots, w_q]$, the eigentensors of $(\hat{C}^0)^+ \cdot \hat{C}^\tau$ can be expressed as a tensor train Ξ with $\Xi = \mathbf{U} \cdot U_X \cdot \Sigma^{-1} \cdot W$, see Line 4 of Algorithm 1. The evaluations of the associated eigenfunctions at all snapshots are then given by the matrix $\Phi = \Xi^\top \cdot \Psi(X)$, see [5]. The corresponding tensor network also breaks down to a simple matrix product, as is shown in Figure 8.

$$\begin{aligned}
\Psi(Z) &= \mathbf{U} \cdot M_Z = \text{Diagram 1} \\
\Psi(X) &= \mathbf{U} \cdot U_X \cdot \Sigma_X \cdot V_X^\top = \text{Diagram 2} \\
\Psi(Y) &= \mathbf{U} \cdot M_Y = \text{Diagram 3}
\end{aligned}$$

Figure 6: Construction of transformed data tensors for AMUSEt: The tensor trains $\Psi(X)$ and $\Psi(Y)$ are extracted from the left-orthonormalized tensor train $\Psi(Z)$. Additionally, $\Psi(X)$ is represented by its global SVD. Again, the cores of \mathbf{U} (as well as U_X) are represented by half-filled circles in blue, Σ by an orange circle, and V_X by a half-filled green circle. The last cores of $\Psi(Z)$ and $\Psi(Y)$ are depicted by a gray and a white circle, respectively.

$$\begin{aligned}
&\mathbf{U} \cdot U_X \cdot \Sigma^{-1} \left\{ \begin{array}{c} \text{Diagram 1} \\ \text{Diagram 2} \\ \text{Diagram 3} \end{array} \right\} \\
&\Psi(Y)^\top \left\{ \begin{array}{c} \text{Diagram 4} \end{array} \right\} \\
&\Psi(X) \left\{ \begin{array}{c} \text{Diagram 5} \end{array} \right\} \\
&\Sigma^{-1} \cdot U_X^\top \cdot \mathbf{U}^\top \left\{ \begin{array}{c} \text{Diagram 6} \end{array} \right\}
\end{aligned}
= \text{Diagram 7}$$

Figure 7: Graphical representation of the reduced matrix: Given the tensors $\Psi(X)$ and $\Psi(Y)$ as depicted in Figure 6, the reduced matrix $M \in \mathbb{R}^{r \times r}$ is computed by contracting the above tensor network. Half-filled circles in blue depict the cores of \mathbf{U} and U_X , while Σ and Σ^{-1} are represented by orange and red circles, respectively.

$$\begin{aligned}
\Xi &= \text{Diagram 1} \\
\Phi &= \text{Diagram 2} = \text{Diagram 3}
\end{aligned}$$

Figure 8: Graphical representation of the eigentensors and eigenfunctions: The tensor train Ξ is built by the contraction of \mathbf{U} , U_X , Σ^{-1} , and W . The matrix Φ comprising the evaluations of the eigenfunctions at the given snapshots is constructed by multiplying the tensors $\Psi(X)$ and Ξ . Similar to the construction of the reduced matrix, see Figure 7, only a few cores remain since the orthonormal cores cancel out and Σ is multiplied by its inverse.

Remark 1: Note that we do not need the cores of \mathbb{U} after the orthonormalization procedure if we are only interested in the approximated eigenfunctions. For both the construction of the reduced matrix M (Figure 7) as well as the eigenfunction evaluations Φ (Figure 8), the TT segment \mathbb{U} is not required due to its orthonormality. In particular, when using the HOSVD approach, this significantly reduces the storage consumption since we are able to construct the left-orthonormalized version of $\Psi(X)$ step by step, i.e., we only need to store two TT cores in memory at the same time.

Example 4: Let us finally apply tEDMD to our guiding example. Table 2 shows the relative 2-norm errors e_λ, e_ξ between the eigenpairs (λ, ξ) computed in Example 1 (using classical EDMD) and their approximations $(\hat{\lambda}, \hat{\xi})$ computed by AMUSEt, using HOSVD or HOCUR, respectively.

Table 2: Application of AMUSEt using HOSVD and HOCUR: For different thresholds (HOSVD) and maximum ranks (HOCUR), respectively, the relative errors of the approximate eigenvalues and eigentensors (in comparison to the matrix case) are shown. For the HOSVD approach, we excluded the threshold 0 because then the pseudoinverse has an extremely high condition number which leads to inaccurate results.

Method	Threshold/maximum rank	1st eigenpair		2nd eigenpair	
		e_λ	e_ξ	e_λ	e_ξ
AMUSEt (HOSVD)	1e-12	6.66e-16	3.53e-13	3.59e-15	3.45e-13
	1e-01	1.96e-04	3.44e-02	2.16e-04	3.60e-02
AMUSEt (HOCUR)	2400	9.82e-05	2.27e-02	1.03e-04	2.30e-02
	2375	1.36e-03	8.92e-02	1.19e-03	9.63e-02
	2350	3.29e-03	1.85e-01	3.46e-03	1.76e-01

We see that both decompositions provide accurate approximations of the eigenvalues and eigenvectors, which motivates the application of AMUSEt to high-dimensional systems. Moreover, Figure 9 shows the approximate eigenfunctions φ_2 and φ_3 .

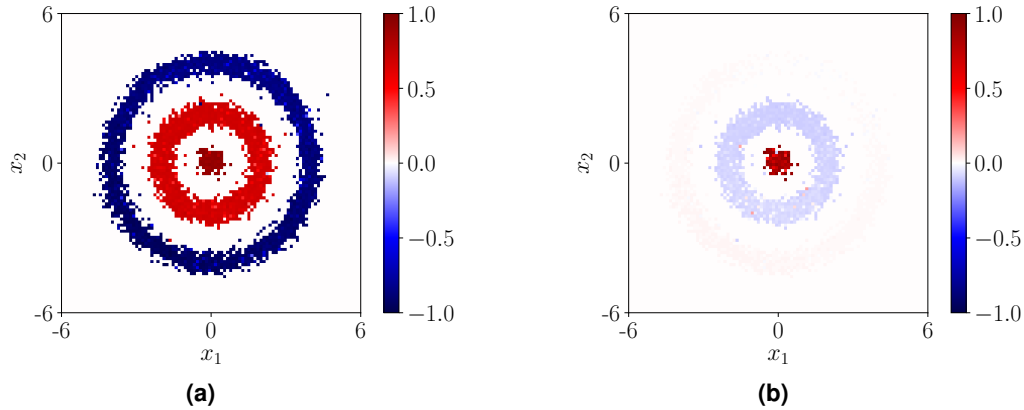


Figure 9: Approximate eigenfunctions of the Koopman operator: (a) Eigenfunction φ_2 defined by $\varphi_2(x) = \Xi_2^\top \cdot \Psi(x)$, $x \in [-6, 6] \times [-6, 6]$, where Ξ_2 is the second eigentensor computed using HOCUR with maximum rank 2350. (b) Eigenfunction φ_3 with analogous construction. The tensor-based results are virtually indistinguishable from those obtained by applying classical AMUSE.

3.5 Subspace interpretation

We show that computing the global SVD of a transformed data tensor (12) amounts to selecting an r_p -dimensional subspace of the full tensor space \mathbb{V} . Application of AMUSEt in fact provides a solution of the Galerkin eigenvalue problem (5) in this subspace. For reversible systems, the variational principle (6) holds in the infinite data limit.

Lemma 1: After k steps of the global SVD algorithm applied to the decomposition (12), core $\Psi^{(k+1)}(X)$, viewed as a matrix in $\mathbb{R}^{r_k \cdot n_{k+1} \times m}$, contains the time series of $r_k \cdot n_{k+1}$ functions of the form

$$\zeta_{k,l_k}(x) \cdot \psi_{k+1,i_{k+1}}(x), \quad l_k = 1, \dots, r_k, \quad i_{k+1} = 1, \dots, n_{k+1},$$

with $\zeta_{k,l_k} \in \bigotimes_{l=1}^k \mathbb{V}^l$ and $\psi_{k+1,i_{k+1}} \in \mathbb{V}^{k+1}$.

Proof: The statement clearly holds for $k = 0$ with $\zeta_{0,1} = 1$, so let us consider a general k and assume it is true for all cores up to $\Psi^{(k)}(X)$. Consider the singular value decomposition $\Psi^k(X) = U_k \cdot \Sigma_k \cdot V_k^\top$. The columns of U_k encode r_k linear combinations of the functions represented by $\Psi^{(k)}(X)$, denote those functions by $\zeta_{k,l_k} \in \bigotimes_{l=1}^k \mathbb{V}^l$ for $l_k = 1, \dots, r_k$. The time series of these functions along the data are given by $U_k^\top \cdot \Psi^{(k)}(X) = \Sigma_k \cdot V_k^\top \in \mathbb{R}^{r_k \times m}$. The scaled right singular vectors thus provide the time series of the basis functions selected during the k th compression step. After contracting $\Sigma_k \cdot V_k^\top$ and the next core, the updated core $\Psi^{(k+1)}(X)$ becomes

$$\begin{aligned} \Psi^{(k+1)}(X)_{l_k, i_{k+1}, t} &= \sum_{t'=1}^m [\Sigma_k V_k^\top]_{l_k, t'} \cdot \delta_{t, t'} \cdot \psi_{k+1, i_{k+1}}(x_t) \\ &= \zeta_{k, l_k}(x_t) \cdot \psi_{k+1, i_{k+1}}(x_t). \end{aligned}$$

Applying this argument p times, it follows that the global left singular vectors \mathbf{U} in Section 3.3 encode an r_p -dimensional subspace of the full tensor space \mathbb{V} , and the tensor $\mathbf{U} \cdot \Sigma^{-1}$ provides a corresponding orthonormal basis. Consequently, solving (16) is equivalent to solving (5) for this subspace. Given some technical assumptions, we can show that the subspace converges in the limit of infinite data:

Proposition 1: Assume that the global SVD algorithm is applied to (12) at fixed ranks r_k , $k = 1, \dots, p$. Moreover, assume that for a sufficient amount of data, the transformed cores $\Psi^{(k)}(X)$ always possess a singular value gap of at least $\delta_k > 0$ between their (r_k) th and (r_{k+1}) th singular value. Then, the subspace represented by \mathbf{U} converges for infinite data size. In the reversible case, the variational principle (6) holds in this limit.

Proof: It suffices to establish convergence of the r_k -dimensional left singular subspace of each reshaped core $\Psi^{(k)}(X) \in \mathbb{R}^{r_{k-1} n_k \times m}$, or equivalently of $\text{span}\{\zeta_{k,l_k}\}_{l_k=1}^{r_k}$. Again, we can apply an inductive argument. Noting that $\zeta_{0,1} = 1$, the claim holds for $k = 0$. Assuming the claim is true for $k - 1$, we note that $\Psi^{(k)}(X) \cdot (\Psi^{(k)}(X))^\top$ converges to the overlap matrix C^0 of the functions $\zeta_{k-1, l_{k-1}} \psi_{k, i_k}$ by ergodicity of the process. Hence the singular values of $\Psi^{(k)}(X)$ converge to the square roots of the eigenvalues of this matrix by the Hoffman–Wielandt theorem [41]. Finally, the assumption on a singular value gap allows to invoke the Davis–Kahan theorem [42] to show convergence of the dominant eigenspace of $\Psi^{(k)}(X) \cdot (\Psi^{(k)}(X))^\top$, which equals the space of leading left singular vectors of $\Psi^{(k)}(X)$. This concludes the proof.

4 Numerical examples

We apply the data-driven tensor-decomposition methods developed in the previous section to two benchmarking data sets of molecular dynamics simulation. Both of these systems have been analyzed before, using standard methods in the field, providing reference values which serve as comparison for our results. We demonstrate that our algorithms enable us to work on large trial spaces where the full calculation of the tensors \hat{C}^0 , \hat{C}^τ is very hard or impossible.

The numerical experiments have been performed on a Linux machine with 128 GB RAM and an Intel Xeon processor with a clock speed of 3 GHz and 8 cores. The algorithms have been implemented in Python 3.6 and collected in the toolbox Scikit-TT¹. Furthermore, we used d3s² as well as PyEMMA³ [43] for simulating and analyzing the numerical examples (including the guiding example).

¹https://github.com/PGelss/scikit_tt

²<https://github.com/sklus/d3s>

³<http://www.emma-project.org>

4.1 Deca-alanine

We re-analyze molecular dynamics simulation data of deca-alanine peptide in explicit water (see [28] for the simulation setup). The original simulation data are downsampled to an effective saving interval of 500 ps, leaving a total of $m = 6000$ frames in the data set. We choose $p = 10$ elementary subspaces \mathbb{V}^k , each of them spanned by either $n_k = 3$ or $n_k = 4$ functions of a single dihedral angle of the peptide. These functions always include the constant and two or three periodic Gaussians of the form

$$\psi_{k,i_k}(x_k) = \exp \left[-\frac{1}{2s_{i_k}} \sin^2(0.5(x_k - c_{i_k})) \right].$$

Their positions and shapes are motivated by the typical distribution of protein data along its backbone dihedral angles, see Figures 10 (a) and (b). We do not include functions of the outermost dihedrals, as these are known to be flexible and not to contribute to the slow dynamics of deca-alanine. The full tensor space \mathbb{V} is of dimension $N = 3^5 \cdot 4^5 \approx 2.5 \cdot 10^5$.

We use the direct decomposition (12) and the HOCUR decomposition (Section 3.2) to arrive at TT representations of the transformed data tensor $\Psi(Z)$. Subsequently, the procedure outlined in Section 3.4 is applied to obtain eigenvalues and eigenfunctions of the reduced problem (16). Following common practice [44], we repeat the procedure for a series of lag times τ , and convert the eigenvalues $\lambda_k(\tau)$ of (16) into estimates for implied timescales, see (3), by the formula

$$t_k = -\frac{\tau}{\log(\lambda_k(\tau))}.$$

We monitor the slowest implied timescale t_2 as a function of τ , and compare the results to a reference Markov state model (MSM). This MSM was built by following the standard protocol of first applying TICA [45] to the dihedral time series, then using k -means to discretize the leading 5 TICA dimensions into 500 discrete sets, and finally estimating an MSM based on this discretization [44].

When working with the HOSVD method, a crucial parameter is the relative truncation threshold ε used during the global SVD calculation. In Figure 10 (c), we compare estimates of t_2 obtained for different values of ε . Several observations can be made: First, most of the results agree well with the reference, even for ε as large as 10^{-3} . It should be noted that the maximal rank of these TT representations differs by about an order of magnitude: for $\varepsilon = 10^{-5}$, we have $r_p = 1018$, while for $\varepsilon = 10^{-3}$, $r_p = 109$. Second, timescale estimates increase as ε decreases. This observation reflects the variational principle shown in Proposition 1, as a smaller threshold leads to a larger subspace selected during the global SVD. Finally, we see that for the smallest threshold $\varepsilon = 10^{-6}$, the timescale estimate breaks down at some point. Most likely, this is an instance of overfitting, as for finite data, choosing a small ε means that too much (noisy) information is retained. Thus, the relative truncation threshold also serves as a regularization parameter.

For HOCUR, a natural hyper-parameter to monitor is the maximal rank allowed in Algorithm 3, while the relative truncation threshold is fixed to $\varepsilon = 10^{-4}$. We find that using a rank as low as 50 provides excellent agreement of the slowest timescale with the reference, see Figure 10 (d). In this example, both methods provide efficient tensor train representations which capture the slow dynamics of the peptide.

4.2 NTL9

The second example we study is a set of four equilibrium molecular dynamics simulations of 39 residue protein NTL9 in explicit water. The data were produced by D. E. Shaw Research on the Anton Supercomputer [46], and have been analyzed many times over the past few years as a benchmarking system. All simulations add up to about 3 ns total simulation time. We downsample the data to an effective time step of 2 ns, the total number m of snapshots left is about 1.4 million. Previous studies (e.g., [47]) have shown that closest heavy-atom distances between residues constitute a good feature set to capture the system’s slow dynamics, which mainly consist of the folding / unfolding of NTL9. Excluding first and second neighbors, this set of descriptors includes 666 distances, but it turns out that only a small fraction of these descriptors is actually required if they are filtered by a simple physical heuristic. We define a contact between two residues

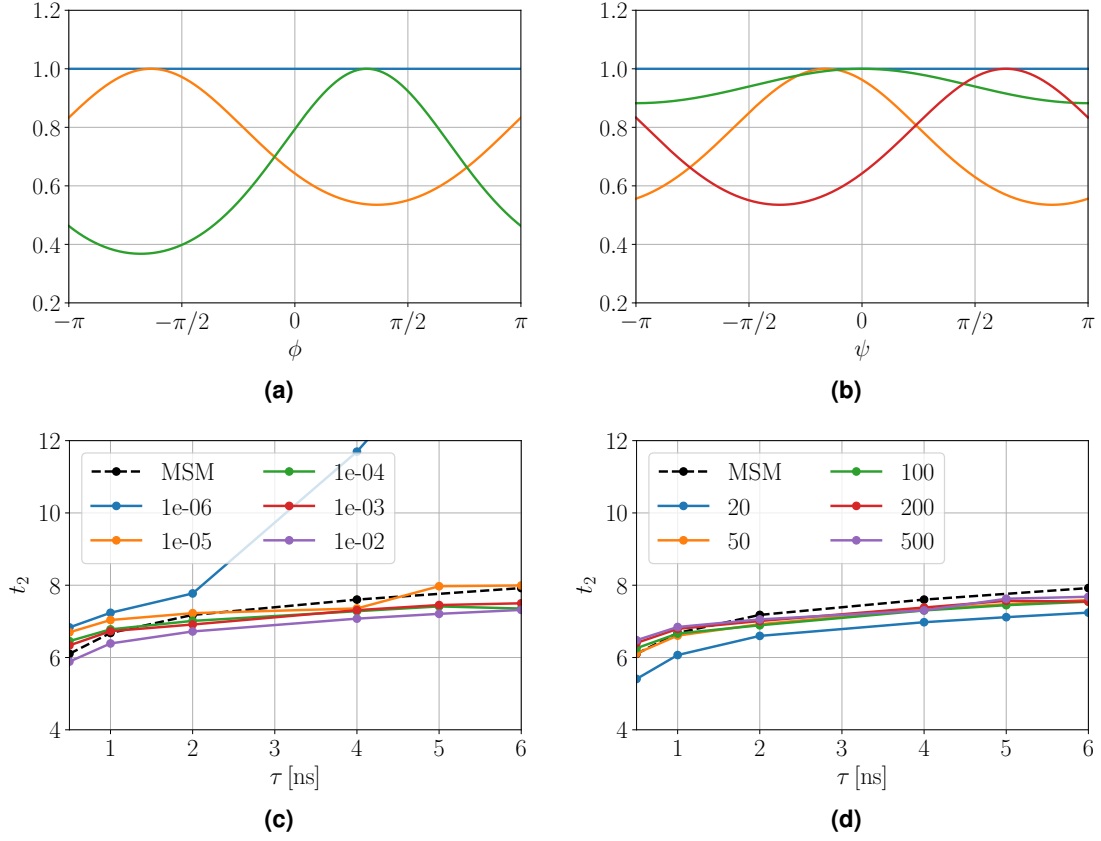


Figure 10: Results for molecular dynamics simulation data of deca-alanine peptide: (a) Univariate basis set used for all ϕ -dihedral angles, comprised of the constant and periodic Gaussians centered at $c_{i_k} = \{-2, 1\}$, with $s_{i_k} = \{0.8, 0.5\}$. (b) The same for all ψ -dihedral angles, where periodic Gaussians are centered at $c_{i_k} = \{-0.5, 0.0, 2.0\}$, with $s_{i_k} = \{0.8, 4.0, 0.8\}$. (c) Slowest timescale t_2 obtained from (16) after constructing $\Psi(Z)$ using the exact TT decomposition given in (12). We show results for different values of relative SVD truncation parameter ε and as a function of the lag time τ . The reference MSM is represented by the black line. (d) The same if $\Psi(Z)$ is represented by the HOCUR algorithm, for different values of the maximal rank in Algorithm 3.

to have formed if their distance is smaller than 0.35 nm. We can then rank all distances by the fraction of simulation time during which the contact was formed. It turns out that using only the ten distances with highest contact probability is enough to build a kinetic model that captures the folding process.

The aim here is not to outperform all existing methods, the point of this example is rather to test the capabilities and limitations of both tensor decompositions presented in this work as the tensor dimension p and the number of snapshots m are increased. The MSM analysis presented in [47] actually provides a more refined model than all the tensor-based approximations we show here. However, the construction of an MSM requires a higher level of expertise and user intervention than our methods. A more natural comparison is the direct application of TICA [45] to a varying number of distance coordinates. This will help us illustrate the value of using a non-linear basis set as opposed to linear models obtained from TICA.

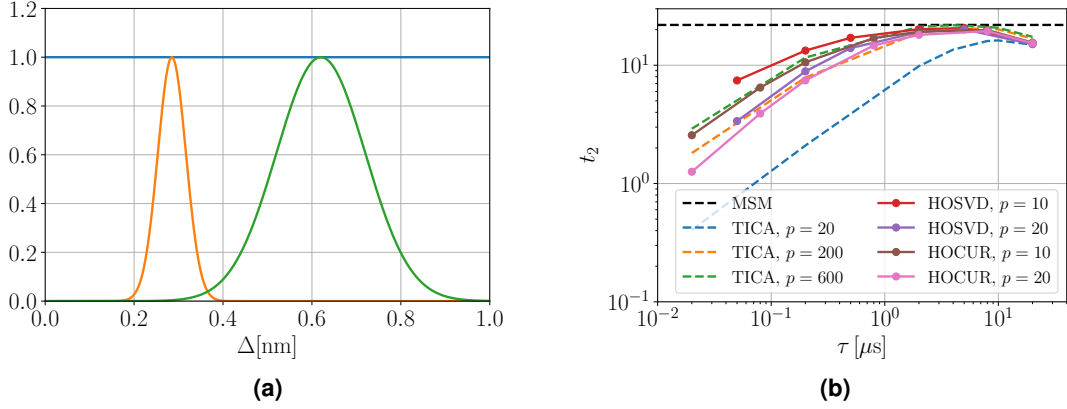


Figure 11: Results for molecular dynamics simulation data of NTL9 protein: (a) Univariate basis set used for all distance coordinates, comprised of the constant and Gaussian functions centered at $c_{i_k} = \{0.285, 0.62\}$, with $s_{i_k} = \{0.001, 0.01\}$. (b) Slowest timescale obtained from (16) after representing the data tensor $\Psi(Z)$ either using the exact decomposition (blue line) or by Algorithm 3 (orange line). For the direct method, we consider approximately 56000 data points, while more than $1.4 \cdot 10^6$ data points were used for HOCUR. The MSM-based reference value as well as the timescales computed by TICA are indicated by the dashed lines.

The elementary functions spaces \mathbb{V}^k are again defined by the constant and two Gaussian functions of the form

$$\psi_{k,i_k}(x_k) = \exp \left[-\frac{1}{2s_{i_k}}(x_k - c_{i_k})^2 \right],$$

centered along each distance coordinate x_k , see Figure 11 (a). We thus have $n_k = 3$ for $k = 1, \dots, p$. The parameters of the Gaussian functions were chosen so that the distribution over all distances in the available data can be reproduced by a linear combination of these basis functions. Just as before, we use both the direct decomposition (12) and the HOCUR iteration to represent the data tensor $\Psi(Z)$. For a series of lag times τ , global SVD at relative truncation parameter $\varepsilon = 10^{-3}$ is then applied to $\Psi(X)$ and the reduced matrix M (16) is computed. After diagonalizing M , we extract estimates of the slowest timescale t_2 and evaluate the first two eigenfunctions on the data as shown in Figure 8.

When using the direct decomposition described in Section 3.1, the major computational bottleneck is the repeated application of SVDs to large matrices. In this example, we find it necessary to downsample the data even further with downsampling rate $\gamma = 25$, bringing the data size down to $m \approx 56000$ corresponding to an effective time step of 50 ns. In this case, we are able to carry out the procedure using the $p = 10, 20$ highest ranked distances (ranked by contact probability), corresponding to a basis set of size $N = 3^{10} = 59049$ and $N = 3^{20} \approx 3.5 \cdot 10^9$, respectively. In Figure 11 (b), we monitor the estimated slowest timescale t_2 as a function of the lag time, and find it indeed to converge towards the reference value with increasing lag time. In this setup, we can run the algorithm within a few minutes. However, we cannot increase the number of distances or

the data size much beyond these limits without a significant increase of computational time and memory requirement.

Interestingly, we can push these limitations further when working with the HOCUR iteration, as it only requires the evaluation of a limited number of tensor entries during the course of the algorithm. We find that the iteration still completes within less than 45 minutes if the $p = 10$ highest ranked distances are used, without any additional downsampling of the data, i.e., $\gamma = 1$. If we set $p = 20$, the computational time needed for the application of AMUSEt is approximately 75 minutes. The corresponding timescales are also found to converge to the MSM reference value, see Figure 11 (b). We note that it takes at least 200 distances to achieve the same approximation quality as any of the tensor-based models if linear TICA is used. When using only 20 distances for TICA, the computed timescales barely approach the reference value obtained by applying MSM. The fact that we can use HOCUR to analyze a large data set of a complex system using a huge number of basis functions ($N = 3^{20}$) on limited computational resources is indeed an encouraging result. Moreover, the maximum rank for the HOCUR approach is much smaller than the TT ranks of the (left-orthonormalized) transformed data tensors produced by the HOSVD approach. That is, the maximum ranks for the application of Algorithm 3 are set to 1000 while the resulting maximum rank of the direct decomposition (12) after left-orthonormalization is larger than 3600.

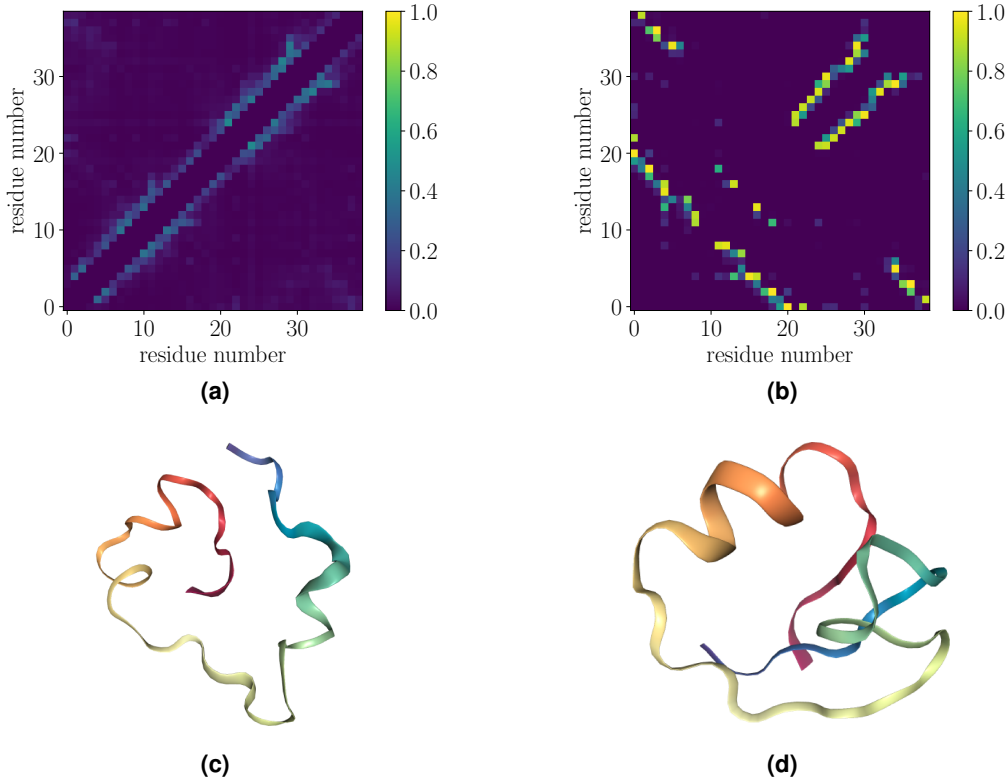


Figure 12: States of NTL9: (a) Contact map for the unfolded state computed from the first two eigenfunctions of the HOCUR model at lag time $\tau = 5 \mu\text{s}$ (upper left triangle), compared to the corresponding contact map of the reference MSM (lower right triangle). (b) The same for the folded state. (c)/(d) Representative molecular structures for the unfolded and folded state of NTL9.

For completeness, we also verify that the second eigenfunction estimated by AMUSEt correctly encodes the folding process of NTL9. To this end, we apply PCCA [48] to the time series of the first two eigenfunctions and assign each snapshot to one of two metastable states if the degree of membership exceeds 0.5. We calculate the contact probabilities separately for each of the two states. These so-called contact maps are shown in the upper left triangles of Figures 12 (a) and (b). By comparing to the contact maps provided by the reference model (lower right triangles in Figures 12 (a) and (b)), we see that there is virtually no difference. In Figures 12 (c) and (d), we also show representative structures for the unfolded and folded state, respectively. The results

shown in Figures 12 are based on the HOCUR model at $p = 20$, but we have verified that the same results can be obtained if the direct model is analyzed.

5 Summary

We have presented different techniques to approximate the Koopman operator associated with high-dimensional dynamical systems using tensor-structured basis sets. Two tensor train representations of the transformed data tensor for such a basis set were introduced. We have provided a detailed algorithmic description of an iterative method to compute a higher-order CUR decomposition, which only requires evaluations of the basis set on the data. Moreover, we have derived an efficient method to solve the eigenvalue problem for the Koopman operator based on TT representations of the data. The size of the resulting matrix eigenvalue problem does not exceed the number of snapshots in the data. A physical interpretation of the method was provided, and we have presented successful applications to two benchmarking data sets of molecular dynamics simulation. In one of these examples, we found that HOCUR decompositions were still able to provide accurate solutions in a setting where the direct HOSVD based method would become intractable. To the best of our knowledge, we have presented the first application of HOCUR in the field of the data-driven analysis of dynamical systems.

Acknowledgements

This research has been funded by the National Science Foundation (CHE-1265929, CHE-1738990, CHE-1900374, PHY-1427654) [FN, CC], the Welch Foundation (C-1570) [FN, CC], the Rice University Academy of Fellows [FN], Deutsche Forschungsgemeinschaft (CRC 1114, “*Scaling Cascades in Complex Systems*”) [PG, SK], and the Einstein Foundation Berlin [CC]. The authors are grateful to D. E. Shaw Research for providing the NTL9 simulation data.

References

- [1] C. Schütte, A. Fischer, W. Huisinga, and P. Deuflhard. A direct approach to conformational dynamics based on hybrid Monte Carlo. *Journal of Computational Physics*, 151(1):146–168, 1999. doi:10.1006/jcph.1999.6231.
- [2] M. Dellnitz and O. Junge. On the approximation of complicated dynamical behavior. *SIAM Journal on Numerical Analysis*, 36(2):491–515, 1999. doi:10.1137/S0036142996313002.
- [3] C. W. Rowley, I. Mezić, S. Bagheri, P. Schlatter, and D. S. Henningson. Spectral analysis of nonlinear flows. *Journal of Fluid Mechanics*, 641:115–127, 2009. doi:10.1017/S0022112009992059.
- [4] M. Budišić, R. Mohr, and I. Mezić. Applied Koopmanism. *Chaos: An Interdisciplinary Journal of Nonlinear Science*, 22(4):047510, 2012. doi:10.1063/1.4772195.
- [5] S. Klus, F. Nüske, P. Koltai, H. Wu, I. Kevrekidis, C. Schütte, and F. Noé. Data-driven model reduction and transfer operator approximation. *Journal of Nonlinear Science*, 28(3):985–1010, 2018. doi:10.1007/s00332-017-9437-7.
- [6] M. O. Williams, I. G. Kevrekidis, and C. W. Rowley. A data-driven approximation of the Koopman operator: Extending dynamic mode decomposition. *Journal of Nonlinear Science*, 25(6):1307–1346, 2015. doi:10.1007/s00332-015-9258-5.
- [7] S. Klus, P. Koltai, and C. Schütte. On the numerical approximation of the Perron–Frobenius and Koopman operator. *Journal of Computational Dynamics*, 3(1):51–79, 2016. doi:10.3934/jcd.2016003.
- [8] F. Noé and F. Nüske. A variational approach to modeling slow processes in stochastic dynamical systems. *Multiscale Modeling & Simulation*, 11:635–655, 2013. doi:10.1137/110858616.
- [9] F. Nüske, B. G. Keller, G. Pérez-Hernández, A. S. J. S. Mey, and F. Noé. Variational approach to molecular kinetics. *Journal of Chemical Theory and Computation*, 10:1739–1752, 2014. doi:10.1021/ct4009156.

- [10] M. O. Williams, C. W. Rowley, and I. G. Kevrekidis. A kernel-based method for data-driven Koopman spectral analysis. *Journal of Computational Dynamics*, 2(2):247–265, 2015. doi:10.3934/jcd.2015005.
- [11] S. Klus, I. Schuster, and K. Muandet. Eigendecompositions of transfer operators in reproducing kernel Hilbert spaces. *ArXiv e-prints*, 2017. arXiv:1712.01572v2.
- [12] A. Mardt, L. Pasquali, H. Wu, and F. Noé. VAMPnets for deep learning of molecular kinetics. *Nature communications*, 9(1):5, 2018. doi:10.1038/s41467-017-02388-1.
- [13] J. D. Carroll and J. J. Chang. Analysis of individual differences in multidimensional scaling via an N-way generalization of ‘Eckart-Young’ decomposition. *Psychometrika*, 35(3):283–319, 1970. doi:10.1007/BF02310791.
- [14] L. R. Tucker. The extension of factor analysis to three-dimensional matrices. In H. Gulliksen and N. Frederiksen, editors, *Contributions to mathematical psychology*, pages 110–127. Holt, Rinehart and Winston, 1964.
- [15] W. Hackbusch and S. Kühn. A new scheme for the tensor representation. *Journal of Fourier analysis and applications*, 15(5):706–722, 2009. doi:10.1007/s00041-009-9094-9.
- [16] I. Oseledets and E. Tyrtyshnikov. Breaking the curse of dimensionality, or how to use SVD in many dimensions. *SIAM Journal on Scientific Computing*, 31(5):3744–3759, 2009. doi:10.1137/090748330.
- [17] I. Oseledets. Tensor-train decomposition. *SIAM Journal on Scientific Computing*, 33:2295–2317, 2011. doi:10.1137/090752286.
- [18] I. Affleck, T. Kennedy, E. H. Lieb, and H. Tasaki. Rigorous results on valence-bond ground states in antiferromagnets. *Physical Review Letters*, 59(7):799–802, 1987. doi:10.1103/PhysRevLett.59.799.
- [19] S. Östlund and S. Rommer. Thermodynamic limit of density matrix renormalization. *Physical Review Letters*, 75(19):3537, 1995. doi:10.1103/PhysRevLett.75.3537.
- [20] M. H. Beck, A. Jäckle, G. A. Worth, and H. D. Meyer. The multiconfiguration time-dependent Hartree (MCTDH) method: a highly efficient algorithm for propagating wavepackets. *Physics Reports*, 324:1–105, 2000. doi:10.1016/S0370-1573(99)00047-2.
- [21] S. Dolgov and B. Khoromskij. Simultaneous state-time approximation of the chemical master equation using tensor product formats. *Numerical Linear Algebra with Applications*, 22(2):197–219, 2015. doi:10.1002/nla.1942.
- [22] P. Gelß, S. Matera, and C. Schütte. Solving the master equation without kinetic Monte Carlo. *Journal of Computational Physics*, 314(C):489–502, 2016. doi:10.1016/j.jcp.2016.03.025.
- [23] Z. Zhang, K. Batselier, H. Liu, L. Daniel, and N. Wong. Tensor computation: A new framework for high-dimensional problems in EDA. *IEEE Transactions on Computer-Aided Design of Integrated Circuits and Systems*, 36(4):521–536, 2017. doi:10.1109/TCAD.2016.2618879.
- [24] P. Gelß, S. Klus, J. Eisert, and C. Schütte. Multidimensional approximation of nonlinear dynamical systems. *Journal of Computational and Nonlinear Dynamics*, 14(6):061006, 2019. doi:10.1115/1.4043148.
- [25] S. Szalay, M. Pfeffer, V. Murg, G. Barcza, F. Verstraete, R. Schneider, and Ö Legeza. Tensor product methods and entanglement optimization for ab initio quantum chemistry. *International Journal of Quantum Chemistry*, 115(19):1342–1391, 2015. doi:10.1002/qua.24898.
- [26] F. Litzinger, L. Boninsegna, H. Wu, F. Nüske, R. Patel, R. Baraniuk, F. Noé, and C. Clementi. Rapid calculation of molecular kinetics using compressed sensing. *Journal of Chemical Theory and Computation*, 14(5):2771–2783, 2018. doi:10.1021/acs.jctc.8b00089.
- [27] S. Klus and C. Schütte. Towards tensor-based methods for the numerical approximation of the Perron–Frobenius and Koopman operator. *Journal of Computational Dynamics*, 3(2):139–161, 2016. doi:10.3934/jcd.2016007.
- [28] F. Nüske, R. Schneider, F. Vitalini, and F. Noé. Variational tensor approach for approximating the rare-event kinetics of macromolecular systems. *Journal of Chemical Physics*, 144(5):054105, 2016. doi:10.1063/1.4940774.
- [29] L. Tong, V. C. Soon, Y. F. Huang, and R. Liu. AMUSE: a new blind identification algorithm. In *IEEE international symposium on circuits and systems*, pages 1784–1787. IEEE, 1990. doi:10.1109/ISCAS.1990.111981.
- [30] S. Klus, P. Gelß, S. Peitz, and C. Schütte. Tensor-based dynamic mode decomposition. *Nonlinearity*, 31(7), 2018. doi:10.1088/1361-6544/aabc8f.

- [31] I. Oseledets and E. Tyrtshnikov. TT-cross approximation for multidimensional arrays. *Linear Algebra and its Applications*, 432(1):70–88, 2010. doi:10.1016/j.laa.2009.07.024.
- [32] G. Froyland, C. P. Rock, and K. Sakellariou. Sparse eigenbasis approximation: Multiple feature extraction across spatiotemporal scales with application to coherent set identification. *Communications in Nonlinear Science and Numerical Simulation*, 77:81–107, 2019. doi:10.1016/j.cnsns.2019.04.012.
- [33] R. Penrose. Applications of negative dimensional tensors. *Combinatorial mathematics and its applications*, 1:221–244, 1971.
- [34] P. Gelß, S. Klus, S. Matera, and C. Schütte. Nearest-neighbor interaction systems in the tensor-train format. *Journal of Computational Physics*, 341:140–162, 2017. doi:10.1016/j.jcp.2017.04.007.
- [35] S. A. Goreinov, E. E. Tyrtshnikov, and N. L. Zamarashkin. A theory of pseudoskeleton approximations. *Linear Algebra and its Applications*, 261(1):1–21, 1997. doi:10.1016/S0024-3795(96)00301-1.
- [36] G. W. Stewart. Four algorithms for the efficient computation of truncated pivoted QR approximations to a sparse matrix. *Numerische Mathematik*, 83(2):313–323, 1999. doi:10.1007/s002110050451.
- [37] C. Boutsidis and D. P. Woodruff. Optimal CUR matrix decompositions. In *Proceedings of the Forty-sixth Annual ACM Symposium on Theory of Computing*, STOC '14, pages 353–362. ACM, 2014. doi:10.1145/2591796.2591819.
- [38] S. A. Goreinov, I. V. Oseledets, D. V. Savostyanov, E. E. Tyrtshnikov, and N. L. Zamarashkin. How to find a good submatrix. In *Matrix Methods: Theory, Algorithms And Applications: Dedicated to the Memory of Gene Golub*, pages 247–256. World Scientific, 2010. doi:10.1142/9789812836021_0015.
- [39] S. A. Goreinov and E. E. Tyrtshnikov. The maximal-volume concept in approximation by low-rank matrices. In V. Olshevsky, editor, *Structured Matrices in Mathematics, Computer Science, and Engineering I*, volume 280, pages 47–51. American Mathematical Society, 2001. doi:10.1090/conm/280/4620.
- [40] S. V. Dolgov, B. N. Khoromskij, I. V. Oseledets, and D. V. Savostyanov. Computation of extreme eigenvalues in higher dimensions using block tensor train format. *Computer Physics Communications*, 185(4):1207–1216, 2014. doi:10.1016/j.cpc.2013.12.017.
- [41] E. E. Tyrtshnikov. *A brief introduction to numerical analysis*. Birkhäuser Basel, 1997. doi:10.1007/978-0-8176-8136-4.
- [42] G. W. Stewart and J. Sun. *Matrix perturbation theory*. Computer science and scientific computing. Academic Press, 1990.
- [43] M. K. Scherer, B. Trendelkamp-Schroer, F. Paul, G. Pérez-Hernández, M. Hoffmann, N. Plattner, C. Wehmeyer, J.-H. Prinz, and F. Noé. PyEMMA 2: A software package for estimation, validation, and analysis of Markov models. *Journal of Chemical Theory and Computation*, 11(11):5525–5542, 2015. doi:10.1021/acs.jctc.5b00743.
- [44] G. R. Bowman, V. S. Pande, and F. Noé, editors. *An introduction to Markov state models and their application to long timescale molecular simulation*. Springer Netherlands, 2014. doi:10.1007/978-94-007-7606-7.
- [45] G. Pérez-Hernández, F. Paul, T. Giorgino, G. De Fabritiis, and F. Noé. Identification of slow molecular order parameters for Markov model construction. *Journal of Chemical Physics*, 139(1):15102, 2013. doi:10.1063/1.4811489.
- [46] K. Lindorff-Larsen, S. Piana, R. O. Dror, and D. E. Shaw. How fast-folding proteins fold. *Science*, 334(6055):517–520, 2011. doi:10.1126/science.1208351.
- [47] L. Boninsegna, R. Banisch, and C. Clementi. A data-driven perspective on the hierarchical assembly of molecular structures. *Journal of Chemical Theory and Computation*, 14(1):453–460, 2017. doi:10.1021/acs.jctc.7b00990.
- [48] P. Deuffhard and M. Weber. Robust Perron cluster analysis in conformation dynamics. *Linear Algebra and its Applications*, 398:161–184, 2005. doi:10.1016/j.laa.2004.10.026.